The Astrophysical Journal, 967:84 (12pp), 2024 June 1 https://doi.org/10.3847/1538-4357/ad40a4

Dependence of Lunar Pickup Ion Flux on Source Location: ARTEMIS Observations

Han-Wen Shen[1], Jasper S. Halekas[1], and Andrew R. Poppe[2]
[1] Department of Physics and Astronomy, University of Iowa, Iowa City, IA, USA; han-wen-shen@uiowa.edu
[2] Space Sciences Laboratory, University of California at Berkeley, Berkeley, CA, USA
Received 2024 February 2; revised 2024 April 9; accepted 2024 April 17; published 2024 May 21

Abstract

The Moon is enveloped in an exosphere, which is comprised of a variety of neutral atoms and molecules. Once exospheric neutrals are ionized by photons, protons, or electrons from the Sun, the resulting ions are accelerated by the electromagnetic fields of their surroundings and can thereby travel away from their source locations. These ions are the so-called pickup ions and are frequently observed by the two Acceleration, Reconnection, Turbulence, and Electrodynamics of Moon's Interaction with the Sun (ARTEMIS) spacecraft. In this study, we identify 115 events from an 11 yr period of ARTEMIS observations, which contain a total of 11,987 samples for our statistics. By using analytical ion trajectory calculations, we trace the source location of each pickup ion observation. Most pickup ion trajectories originate near the subsolar point, consistent with the efficiency of sputtering. We find that the flux of pickup ions strongly anticorrelates with the source altitude, providing indirect evidence of decreasing exospheric ion flux with increasing altitude. We also find that the flux of pickup ions does not show a significant relationship with the crustal magnetic field intensity. This implies that a depression of sputtering efficiency or the trapping of near-surface freshly born ions by a crustal magnetic anomaly may not reduce the subsequent pickup ion flux as effectively as expected. In summary, the present paper provides a statistical view of lunar pickup ion fluxes in association with the altitude, local time, and local crustal magnetic field of their source locations.

Unified Astronomy Thesaurus concepts: The Moon (1692); Lunar science (972); Solar wind (1534); Space plasmas (1544)

1. Introduction

The Moon, the natural satellite of Earth, does not possess a thick atmosphere, but it is surrounded by a collisionless surface-bounded exosphere (Stern 1999). This exosphere has aroused intense attention from the planetary science community since the Apollo era. A full knowledge of exospheric composition, sources, and processes is important for our understanding of the evolution of the lunar environment. The lunar exosphere is composed of a variety of neutral species. Through multiple in situ measurements and remote spectroscopic experiments (e.g., Hoffman et al. 1973; Freeman & Benson 1977; Potter & Morgan 1988; Feldman & Morrison 1991; Mendillo et al. 1991; Flynn & Stern 1996), the most abundant species in the exosphere to date are thought to be helium (He) and argon (Ar). These neutral species have been confirmed by measurements from the Neutral Mass Spectrometer on board the Lunar Atmosphere and Dust Environment Explorer (LADEE) mission, which was the first spacecraft designed especially for the exploration of the lunar exosphere (Elphic et al. 2014; Mahaffy et al. 2014). LADEE also detected known species such as sodium (Na) and potassium (K) (Colaprete et al. 2016a; Szalay et al. 2016; Kuruppuaratchi et al. 2018; Rosborough et al. 2019), as well as some species that had not been detected in the past, such as neon (Ne), aluminum (Al), titanium (Ti), and magnesium (Mg) (Benna et al. 2015; Colaprete et al. 2016b). These exospheric neutrals are inferred to be produced by several processes, including radiogenic outgassing, thermal desorption, photon-stimulated desorption, sputtering by solar wind protons and alphas, and micrometeoroid bombardment (Stern 1999; Yakshinskiy & Madey 1999; Sarantos et al. 2012b; Vorburger et al. 2014).

In addition to the direct detection of neutrals, pickup ion observations have provided another useful approach to reveal the composition and structure of the lunar exosphere and surface (e.g., Hartle & Killen 2006; Hartle et al. 2011). Some mechanisms can produce ions around the Moon, including direct sputtering from the surface, electron impact ionization, solar wind charge exchange, and photoionization of neutrals (Stern 1999; Hartle & Killen 2006). Once these ions are born, the ambient electromagnetic fields will cause them to either impact the lunar surface or to be accelerated from their source locations along cycloidal trajectories in the plane of the electric field (Cladis et al. 1994). The ions carried away by the electric field are called pickup ions. Lunar pickup ions are mostly observed in the solar wind because the combination of the solar wind convection velocity and interplanetary magnetic field can typically lead to a large motional electric field on the order of a few millivolts per meter. In addition to the solar wind environment, freshly born ions can be picked up in any environment where a motional electric field is present, such as the terrestrial magnetosheath and magnetotail.

So far, lunar pickup ions have been detected both near to and remote from the Moon by various missions, including Active Magnetospheric Particle Tracer Explorers (AMPETE; Hilchenbach et al. 1993), Wind (Mall et al. 1998), Kaguya (Tanaka et al. 2009; Yokota et al. 2009), Chang'e-1 (Wang et al. 2011; Zhong et al. 2013), LADEE (Halekas et al. 2015; Poppe et al. 2016), and Acceleration, Reconnection, Turbulence, and Electrodynamics of the Moon's Interaction with the Sun (ARTEMIS; Halekas et al. 2012; Poppe et al. 2012; Halekas et al. 2013; Poppe et al. 2013; Zhou et al. 2013; Harada et al. 2015; Halekas et al. 2016; Liuzzo et al. 2021). The studies using data obtained from these missions have confirmed the

existence of multiple ion species, with masses spanning between 2 and 56 amu, and the suggested species include H_2^+, C^+, O^+, CH_4^+, Ne^+, Na^+, Al^+, Si^+, CO^+, N_2^+, K^+, Ar^+, Ca^+, and Fe^+. Many species of lunar pickup ions listed above have not been detected in their neutral form, and pickup ion observations thus fill in a number of gaps in our understanding of the lunar exospheric composition.

Several previous studies have greatly improved our current knowledge about the species of lunar pickup ions; however, some aspects of lunar pickup ions remain incompletely explored. For example, what factors control the flux of lunar pickup ions? Based on a set of 29 pickup ion events observed by the two ARTEMIS probes, Halekas et al. (2012) found that the flux of pickup ions positively correlates with that of solar wind protons, suggesting the importance of sputtering directly and/or indirectly in producing ions from the surface. Halekas et al. (2016) conducted an analytical trajectory analysis on a pickup ion event in which the flux and energy of pickup ions vary with time. Their results suggested a possible asymmetry in the ion production rate between source regions with and without lunar magnetic anomalies. However, more cases or a statistical study are still needed to verify this effect of crustal magnetic anomalies on the flux of pickup ions, and to explore the role of other source location characteristics in determining the flux of pickup ions. In the present study, we select a total of 115 pickup ion events from an 11 yr period (2012–2022) of ARTEMIS observations (only for times when the Moon is exposed to the solar wind). Through analytical ion trajectory calculations, the source location of each pickup ion observation could be traced. We then implement statistical analyses on observed pickup ion fluxes in combination with altitudes, local times, and crustal magnetic field intensities of pickup ion source locations. The rest of this paper is organized as follows. Section 2 presents ARTEMIS observations and demonstrates the identification of pickup ion events. We illustrate our analytical ion trajectory calculations used in the present study in Section 3. In Section 4, we analyze and discuss the relationships of the pickup ion flux with the three potential controlling factors stated above. Finally, we summarize our analyses and draw conclusions in Section 5.

2. ARTEMIS Observations of Lunar Pickup Ions

The ARTEMIS mission consists of two probes, which were redeployed from the five-probe Time History of Events and Macroscale Interactions during Substorms (THEMIS) mission to extend as a mission to the Moon since the end of 2011 (Angelopoulos 2008, 2011). Each of the two ARTEMIS probes has elliptical orbits around the Moon near the equatorial plane, with inclinations of 0°–30°, aposelenes of ~15,000–19,000 km, and periselenes with variable altitudes of 10–1000 km from the lunar surface. Both probes carry identical instruments to conduct comprehensive measurements of charged particles and electromagnetic fields. The fluxgate magnetometer (FGM) measures the magnetic field and its fluctuations from DC to 64 Hz (Auster et al. 2008). The electrostatic analyzer (ESA) consists of two sensors to measure ions and electrons. Both sensors have a $180° \times 6°$ instantaneous field of view, sweeping out 4π steradians per ~4 s spin period (McFadden et al. 2008a, 2008b). During the mission around the Moon, the ESA instruments predominantly operate in magnetospheric mode, enabling pickup ion observations. In magnetospheric mode, the ESA measures ions from 1.6 eV–25 keV in full angular coverage, with ~30% energy resolution and 22.5° angular resolution, to provide three-dimensional particle distributions. A variety of ion moments, as well as time–energy and time–angle spectrograms, are then computed from these particle distributions.

There is a motional electric field $\boldsymbol{E} = -\boldsymbol{U} \times \boldsymbol{B}$ around the lunar environment when the solar wind carries an interplanetary magnetic field $\boldsymbol{B}$ flows past the Moon with a velocity $\boldsymbol{U}$. Lunar pickup ions are then continuously accelerated along $\boldsymbol{E}$ from their birthplaces and follow cycloidal trajectories in the plane that contains $\boldsymbol{E}$ and $\boldsymbol{U}$ and is perpendicular to $\boldsymbol{B}$. Because of the low orbital inclinations of the two ARTEMIS probes, these pickup ion trajectories must lie close to the near-ecliptic planes in order to be easily observed by the two probes. Therefore, the favorable condition for pickup ions to be observed by the ARTEMIS spacecraft is a Z-component dominated $\boldsymbol{B}$ and a Y-component dominated $\boldsymbol{E}$ in Solar Selenocentric Ecliptic (SSE) coordinates. In this coordinate frame, the X-axis points toward the Sun from the Moon, the Z-axis is parallel to the upward normal to the ecliptic plane, and the Y-axis completes the right-handed set.

Figure 1 shows an example event of lunar pickup ions, which was observed by the ARTEMIS probe 2 on 2012 November 1. We use this event to illustrate the defining characteristics of pickup ions observed by an ARTEMIS probe, which are adopted to visually identify all pickup ion observations that are analyzed in the present study. As displayed in Figure 1(a), lunar pickup ions typically have a signal at narrow higher-energy bins well separated from the solar wind proton and alpha particle populations. This feature can help us to rule out most solar wind reflected ions, which instead typically present a relatively broad energy band adjacent to the solar wind component (e.g., Saito et al. 2008; Yokota et al. 2014a; Poppe et al. 2017). In the first step of our event identification process, we search for candidate events from a large number of time–energy spectrograms based on the feature stated above. Pickup ions generally present characteristics of a highly collimated beam that have a relatively narrow energy–angle range, and they thus generally produce a signal in a small number of adjacent energy-angle bins of the ESA measurements (Halekas et al. 2012). For each candidate event identified from a time–energy spectrogram, we manually determine the energy range of pickup ions, as displayed by the two red horizontal lines in Figure 1(a). We then compute the time–phi and time–theta spectrograms for ions in this specific energy range, as displayed by Figures 1(b) and (c). Here, phi and theta represent the azimuthal and polar angles in the spherical DSL (Despun Sun L-vectorZ) coordinate system, respectively. In this coordinate system, the Z-axis is along the spin axis of the spacecraft, the X-axis points from the spacecraft toward the Sun, and the Y-axis completes the triad. From the two angular spectrograms, we can determine whether these ions are restricted to a small number of adjacent angular bins. If so, the angular range of pickup ions is then determined, as indicated by the two pairs of red horizontal lines in Figures 1(b) and (c). From the three-dimensional particle distributions with limits on the specific energy and angular ranges we determined, the total number flux of pickup ions at each observation time can thereby be calculated, as shown in Figure 1(d). In our event identification, we reject events observed during periods with relatively unsteady magnetic and electric fields, in order to reduce the errors caused by the time delays in our subsequent analytical ion trajectory calculations. Based on the 11 yr

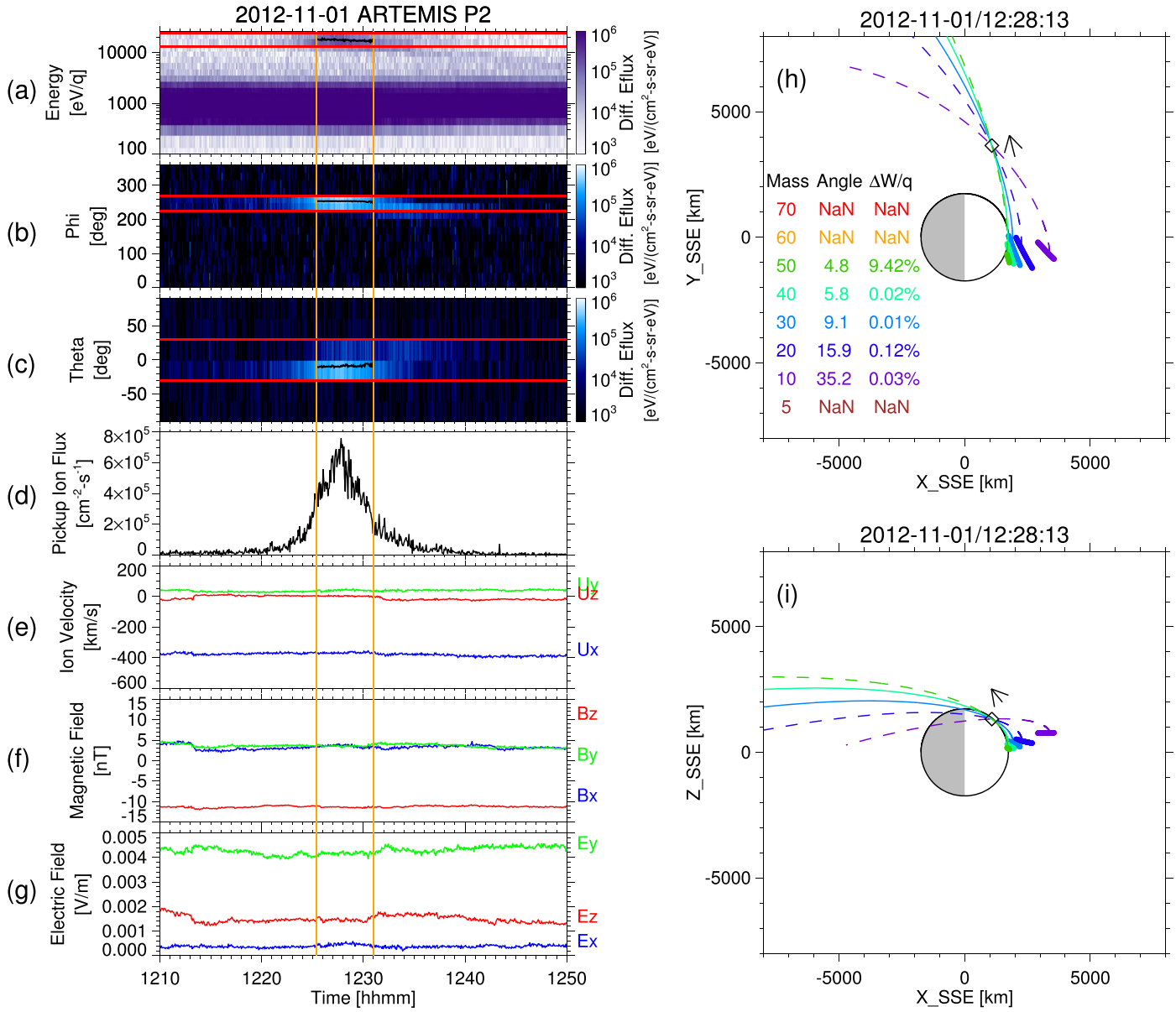

Figure 1. Example of pickup ion event and analytical ion trajectory calculations. The period between the two vertical orange lines in the left-hand panels represents a pickup ion event we identified. (a)–(c) show the time–energy, time–phi, and time–theta spectrograms. The three pairs of red horizontal lines indicate the energy and angular ranges of pickup ions. The black curves in the three spectrograms show the bulk average energy and velocity direction computed from the three-dimensional particle distribution for pickup ions (i.e., ions in the energy and angular ranges indicated by red horizontal lines). (d) exhibits the number flux of pickup ions. (e) and (f) display solar wind velocity and interplanetary magnetic field measured by the ESA and FGM instruments in SSE coordinates, respectively; and the electric field shown in panel (g) is calculated from the cross product of these two vectors. (h) and (i) show the analytically described trajectories of the pickup ion observation sample on 2012 November 1 at 12:28:13 UT. The diamond symbols indicate the location of this sample (i.e., spacecraft position). Trajectories in different colors represent different mass assumptions. For each mass, the points indicate the starting locations of trajectories that can satisfy the altitude constraints described in Section 3 and reach the spacecraft in the correct energy and angular bins (indicated by red horizontal lines in the spectrograms); the trajectory shown is the best one with the minimum difference of the energy and velocity at the observation point from the pickup ion bulk average energy and velocity stated above. If the energy difference is within 5% of the bulk average energy or the difference in the bulk velocity direction is smaller than 10°, this trajectory will be marked by a solid curve; otherwise, it will be marked as a dashed curve and excluded from subsequent analyses. The information on differences in the energy and velocity direction is listed in the lower left of (h).

ARTEMIS observations from 2012–2022, a total of 115 pickup ion intervals are finally identified for our later analyses.

3. Analytical Ion Trajectory Calculations

By tracing pickup ion trajectories back to their source locations, we can possibly clarify the factors that control lunar pickup ion fluxes. To achieve this, we follow the methodology described and applied in the statistical study by Halekas et al. (2012), which somewhat differs from the analogous approach employed in the case study by Halekas et al. (2016). The ambient electromagnetic fields, due to a number of large Alfvén waves passing through the Moon, drastically vary over time during the event analyzed in Halekas et al. (2016). They thus adopted an iterative technique to determine the fields at each given spatial point and time along each ion trajectory, and used a Runge–Kutta method with an adaptive time step to determine the trajectory of each ion

observation. However, similarly to Halekas et al. (2012), we only consider the events in which the fields generally remain steady over a much longer period, enabling us to reasonably assume constant external field conditions for pickup ion trajectories. Therefore, the real-time fields measured by the spacecraft are adopted for our analytical trajectory calculations.

When lunar pickup ions are born, their energies are just a few electronvolts or less. For simplicity, we make a reasonable approximate assumption that these ions are born at zero velocity, i.e., with zero kinetic energy. The freshly born pickup ions follow analytically described cycloidal trajectories (if the fields are uniform and there is not enough turbulence to scatter pickup ion trajectories), and they can be accelerated to up to two times the solar wind speed at the top of cycloids by the solar wind motional electric field. Given a steady and uniform $\boldsymbol{U}$, $\boldsymbol{B}$, and $\boldsymbol{E}$, the characteristic radius and kinetic energy per charge of these trajectories depends on ion mass, with heavier ions having larger radii. It is well known that the gained kinetic energy (δW) per charge (q) by a traveling pickup ion depends on $\boldsymbol{E}$ and the path ($\boldsymbol{r}$) traveled from its source location along this field, which can be written as follows:

$$\delta W/q = \int \boldsymbol{E} \cdot d\boldsymbol{r}.$$

Since it is known that this pickup ion moves only in the plane of $\boldsymbol{U}$ and $\boldsymbol{E}$, the trajectory of this pickup ion can be parameterized in a two-dimensional cycloidal form expressed by the following two equations:

$$X = X_0 + r_g{}^*(\theta - \sin\theta)$$

$$Y = Y_0 + r_g{}^*(1 - \cos\theta)$$

where X_0 and Y_0 indicate the birth point of the pickup ion; X and Y are an observation point in coordinates aligned with the drift velocity $\boldsymbol{U_{perp}} = (\boldsymbol{E}\times\boldsymbol{B})/B^2$ and $\boldsymbol{E}$, respectively; θ represents the gyrophase of the observation point; and $r_g = (m\,{}^*U_{perp})/(q\,{}^*B)$ represents the ion gyroradius, in which m, U_{perp}, and B indicate the ion mass, drift speed, and magnetic field magnitude, respectively. The kinetic energy per charge gained by the pickup ion now can be simplified as a function of gyrophase:

$$\delta W/q = E^*(Y - Y_0) = E^* r_g{}^*(1 - \cos\theta).$$

This quantity is also equal to the net kinetic energy per charge under our assumption that this pickup ion has zero energy when it is born.

To derive analytically described trajectories for each pickup ion observation sample, we use $\boldsymbol{U}$ and $\boldsymbol{B}$ directly measured by the ESA and FGM instruments on board the ARTEMIS spacecraft, respectively, and utilize these two vector quantities to calculate $\boldsymbol{E}$. Since the ESA instruments have no mass-resolving capabilities, we separately derive the possible trajectories for each of eight different ion mass species, including masses of 5, 10, 20, 30, 40, 50, 60, and 70 amu. For each mass species, we divide the gyroangle into 1800 angles with intervals of 0.2° and derive 1800 trajectories for conditions that pickup ions reach the ARTEMIS observation point at different 1800 gyrophases. We reject the trajectories in which the altitude of the birth point from the lunar surface is lower than zero because pickup ions are produced from the surface or exosphere. The densities of most exospheric neutral species estimated by Sarantos et al. (2012a) and Poppe et al. (2022) at regions with distances beyond 4000 km from the center of the Moon typically fall below 10 cm^{-3}, and even less than 1 cm^{-3}. Hence, the trajectories with birth points at these regions are likewise rejected, due to the extremely thin exosphere above that distance. Furthermore, the trajectories that pass through the Moon are ruled out; in other words, the altitude of any point along a reasonable trajectory must be greater than zero. In addition to the altitude constraints described above, the pickup ion velocity and kinetic energy per charge (hereafter referred to as energy or kinetic energy) provide more stringent constraints and criteria on selecting the most likely trajectory from these 1800 trajectories. Pickup ions have different velocity directions and kinetic energies at the ARTEMIS observation point in different trajectories. However, only a subset of the possible trajectories reaches the observation point in the correct energy and angular bins that we have determined from the observed energy and angular spectra, as for the example shown in Figures 1(a)–(c). We select the one trajectory that has the smallest difference from the bulk average energy and velocity direction of pickup ions to trace the source location. Here, the bulk average energy and velocity direction can be computed based on the three-dimensional particle distribution for ions in the determined pickup ion energy and angular ranges, as indicated by black curves in Figures 1(a)–(c). If the energy difference exceeds 5% of the average energy or the difference in the velocity direction is larger than 10°, we will abandon this trajectory. These two thresholds are smaller than half of the instrumental energy and angular resolutions, ensuring that the selected trajectory can better correspond to the peak of the energy/angular response for the bins where pickup ions are seen. In our analytical trajectory calculations, we do not take into account the effect of crustal magnetic fields on altering pickup ion trajectories. Since crustal magnetic fields only have significant magnitudes near the surface, there is only a minor portion at the beginning of trajectories for freshly born ions near the surface that could be affected. It should not lead to significant errors in large-scale ion trajectories.

Figures 1(h) and (i) show an example of analytical ion trajectory calculations for the pickup ion observation at 12:28:13 UT during the event on 2012 November 1. In this case, if the assumed mass of these pickup ions is 5, 60, or 70 amu, there are no analytically described trajectories that can simultaneously meet the altitude constraints defined previously and reach the ARTEMIS probe in the correct energy and angular bins (i.e., the ranges of three pairs of red horizontal lines in Figures 1(a)–(c). Masses between 10 and 20 amu permit the generation of trajectories that satisfy the altitude constraints and reach the probe in the correct energy and angular bins; however, these trajectories do not exhibit alignment at the ARTEMIS observation point within a 10° difference from the direction of the pickup ion bulk average velocity (as displayed by two black arrows in Figures 1(h) and (i)). A mass of 50 amu is unable to produce any trajectory with an energy difference of less than 5% at the observation point compared to the pickup ion bulk average energy (17,787.5 eV q^{-1} at this observation time). Ultimately, only masses of 30 and 40 amu can result in trajectories that well match the observations in this case.

4. Results and Discussion

Figures 2(a) and (b) exhibit the locations of 115 pickup ion events we identified from the ARTEMIS observations in SSE coordinates. As we can see, these ions travel out from the Moon along cycloidal trajectories that lie near the equatorial plane and bend back from the Y-axis. In these 115 events, there

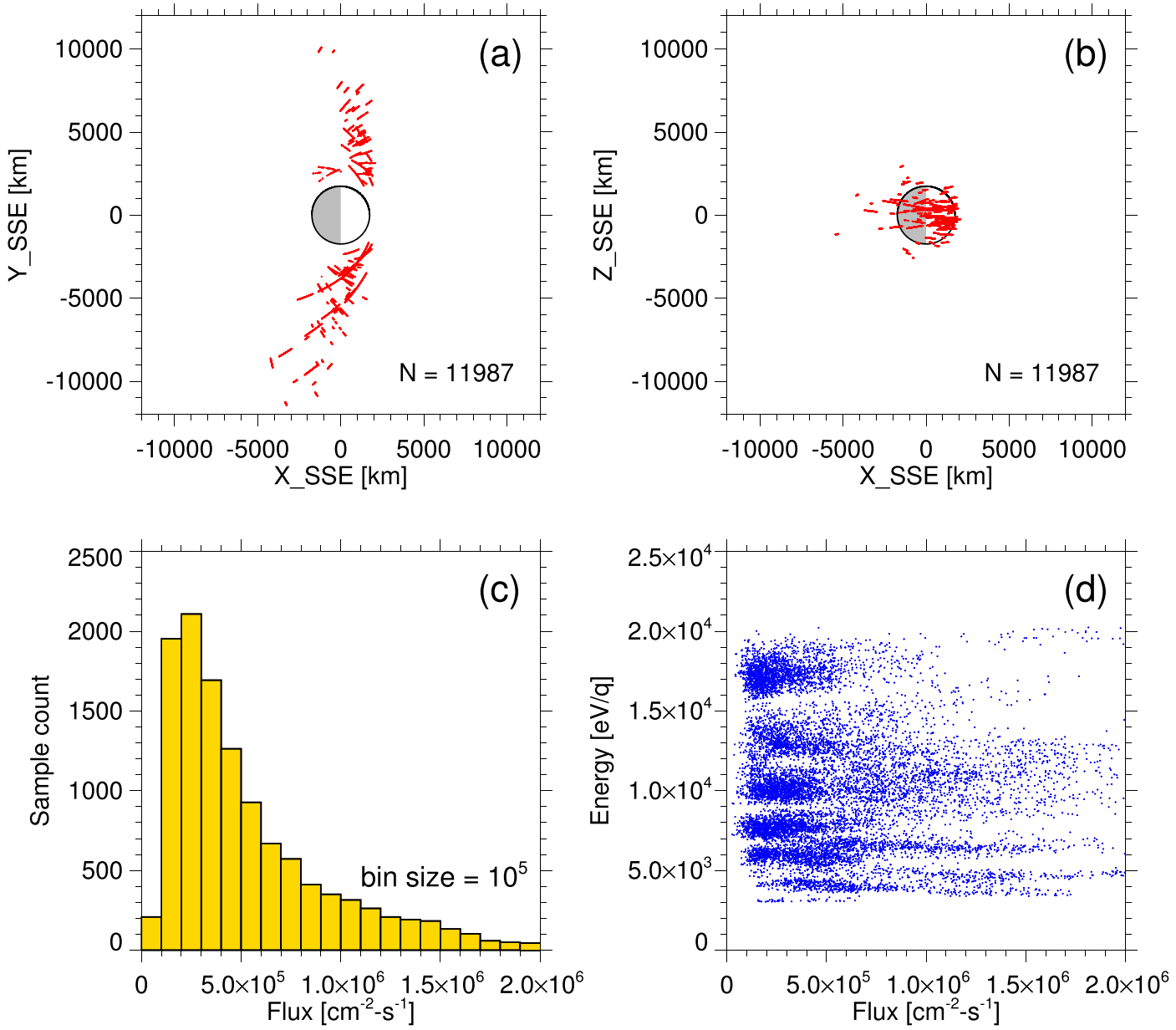

Figure 2. Pickup ion observations by the ARTEMIS spacecraft from 2012–2022. (a) and (b) show the spatial distributions of these observations in SSE coordinates. (c) displays a histogram of the sample count vs. the pickup ion flux. (d) shows a scatter plot of pickup ion fluxes vs. pickup ion bulk average energies.

are a total of 11,987 pickup ion observation samples that can have analytically described trajectories under the assumption of at least one mass species. The number fluxes of these samples mostly fall in a range of 10^5–10^6 cm^{-2} s^{-1}, as displayed in Figure 2(c). These various fluxes have no significant dependence on the pickup ion bulk average energy, as shown in Figure 2(d). For each pickup ion observation sample at a given assumed mass, we attempt to trace an analytically described trajectory using the numerical calculation method described in Section 3. In our trajectory calculations, none of the pickup ion observation samples can be traced by an analytically described trajectory at a mass of 5 amu. A possible reason is that some ion species (usually low-mass ions), with the size of their pickup trajectories comparable to the neutral scale height, make it difficult to form a sharply peaked feature in the spectra for our visual identification of pickup ions. Since light ions generally have relatively small gyro radii, one may argue that there might be no opportunity to observe these ions if the probes were far away from the Moon. However, as shown in Figure 2(a), the events we identified cover not only regions at large distances but also regions close to the Moon, indicating the possibility of detecting light pickup ions by ARTEMIS. As shown in Figure 3, at almost all flux levels, masses of 20 and 30 amu can allow the greatest portion of pickup ion observation samples to have a trajectory that can be well analytically described. This result implies that the mass of most lunar pickup ions likely lies in the range between 20 and 30 amu, close to previous estimates and observations (e.g., Hilchenbach et al. 1993; Halekas et al. 2012; Zhou et al. 2013; Halekas et al. 2015). At masses larger than 40 amu, we note that the flux of pickup ions demonstrates a negative correlation with the percentage of pickup ion observation samples having analytically described trajectories. This indicates that pickup ion observations with higher fluxes are less likely heavier ions. In

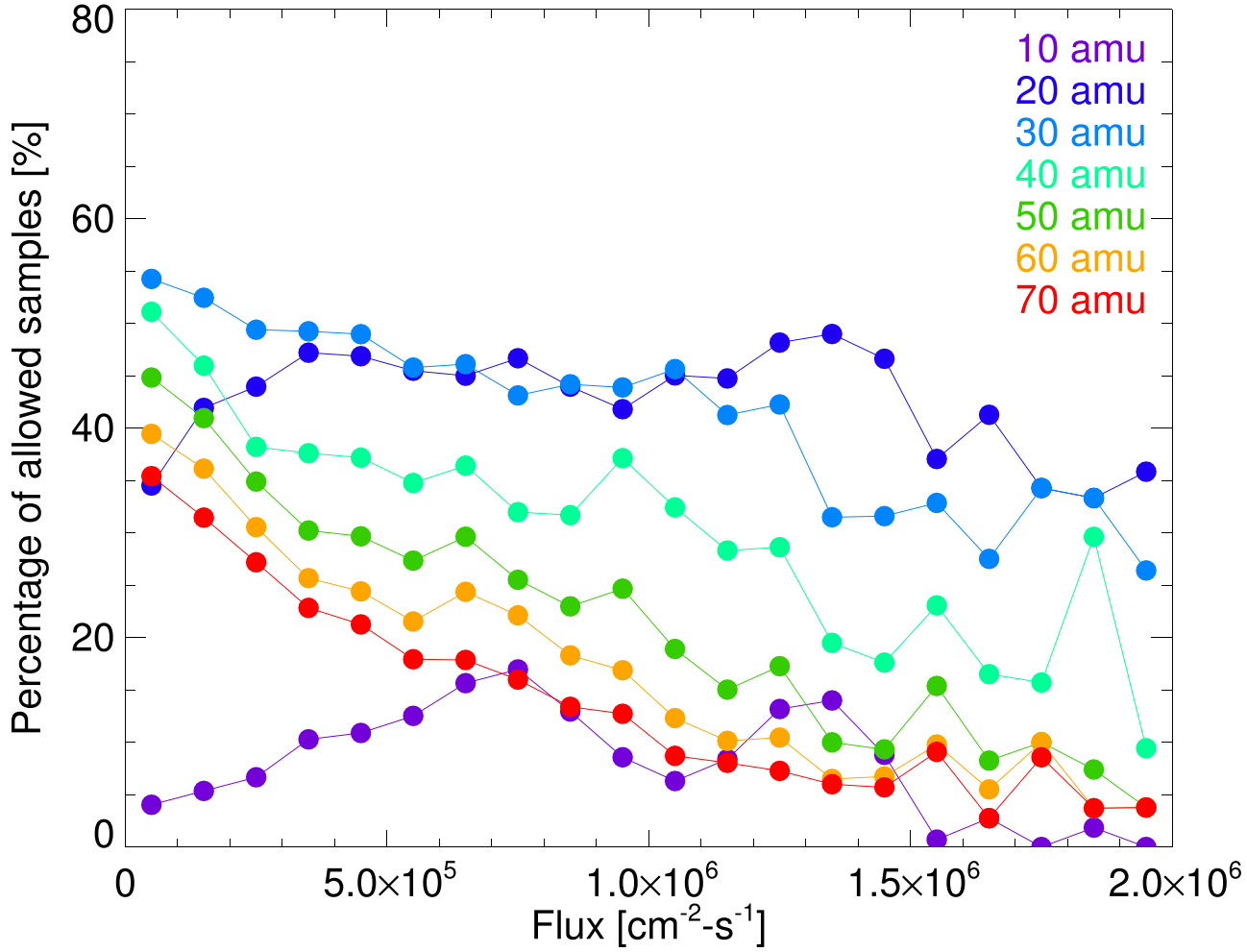

Figure 3. Relationship between the flux and mass of pickup ions. The vertical axis indicates the percentage of pickup ion observation samples with analytically described trajectories at a given assumed mass. Different colors represent different mass assumptions.

the following subsections, for each ion mass species, we statistically analyze the relationship of the flux of pickup ions with each of the source altitude, local time, and crustal magnetic field intensity. It should be noted that these analyzed mass species do not include a mass of 5 amu because no pickup ion observation samples have an analytically described trajectory well consistent with observations at that mass.

4.1. Dependence on Source Local Time

In this subsection, we investigate whether the flux of pickup ions depends on the local time of their source locations. Since each pickup ion observation sample can have different analytically described trajectories under different mass assumptions, the pickup ions could be traced back to slightly different source locations. The first seven panels of Figure 4 individually show scatter plots of pickup ion fluxes versus their source local times for different mass assumptions. The blue curves indicate the median local times as a function of the flux, respectively. The lower and upper bounds of the pink error bars represent the first and third quartiles, respectively. We have also examined the mean curve of each panel (not displayed in this paper), which shows a high similarity to the median curve. The distribution range of data points on the *Y*-axis is wider at smaller fluxes, extending from noon toward dawn and dusk. Overall, the median flux does not significantly vary with local time for each mass species. Most pickup ions originate from the sunlit local times, especially concentrated near noon, in line with the high efficiency of sputtering by solar wind particles at the subsolar point. We also note that the local time distributions for mass species of 10 and 20 amu are slightly biased toward dawn. This could be related to methane (CH_4) and sodium (Na), which have been reported to be more abundant near dawn (Yokota et al. 2014b; Hodges 2016).

4.2. Dependence on Source Altitude

Figure 5 shows the relationship between the flux and source altitude of lunar pickup ions. For any of the seven mass species, the scatter plot of samples demonstrates a negative relation between the two variables. In each panel, the median curve matches the mean curve (not displayed) quite well. We adopt the median values to calculate the Spearman rank correlation coefficient between the flux and source altitude. The correlation coefficients are all negative and lower than −0.8 for all mass species, with six of them as low as at least −0.92, indicating strong anticorrelation between the two examined variables. We have also checked that the associated *p*-values of these correlation coefficients are all smaller than 5%, indicating that they are highly statistically significant (Spearman 1904). As a result, the relationship between the flux and source altitude of pickup ions can be well described by a monotonic function. We compare the median curves of the seven ion mass species in the

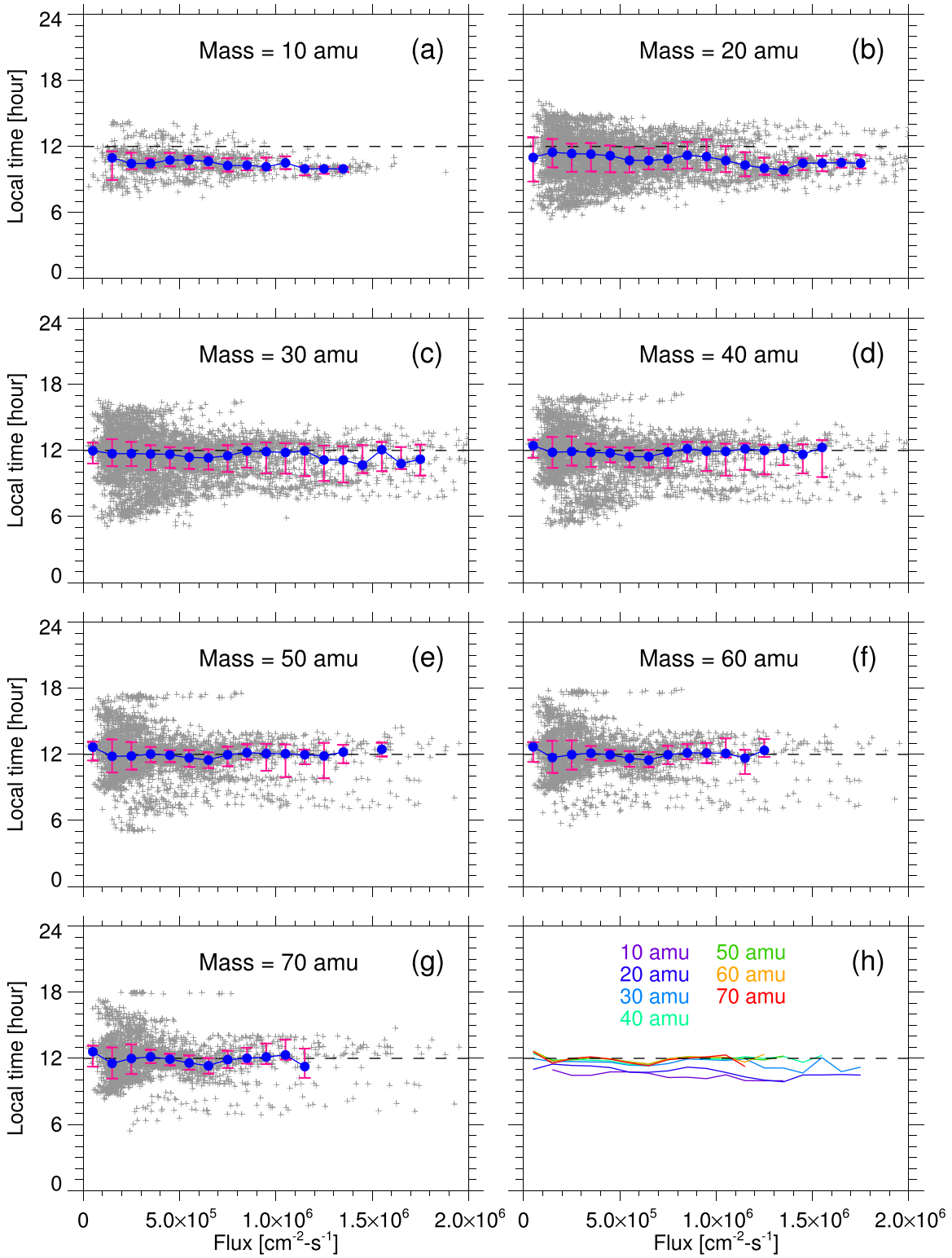

Figure 4. Scatter plots of pickup ion flux vs. source local time. The first seven panels are for seven different ion mass assumptions in the analytical ion trajectory calculations. Blue circles and pink error bars represent the medians and quartiles, respectively. The bin size for calculating medians is 10^5 cm^{-2} s^{-1}. We only calculate the medians and error bars for bins containing a least 20 data points. (h) shows a comparison in the median curve among different mass assumptions.

same panel, as shown in Figure 5(h). These seven curves show the similarity of their trends, but they slightly shift on the vertical axis. Pickup ions with greater masses mostly come from lower altitudes, which seems to reflect a mathematical relationship among energy, gyrophase, and gyroradius for a pickup ion that passes through a given observation point.

Poppe et al. (2022) proposed a comprehensive numerical model for the formation, dynamics, and spatial distributions of lunar pickup ions. There are a total of 25 ion species included in their model, with masses spanning from 2–56 amu (demonstrated in Figure 5(b) of their paper). The production rate of each lunar ion species in the exosphere has a decreasing

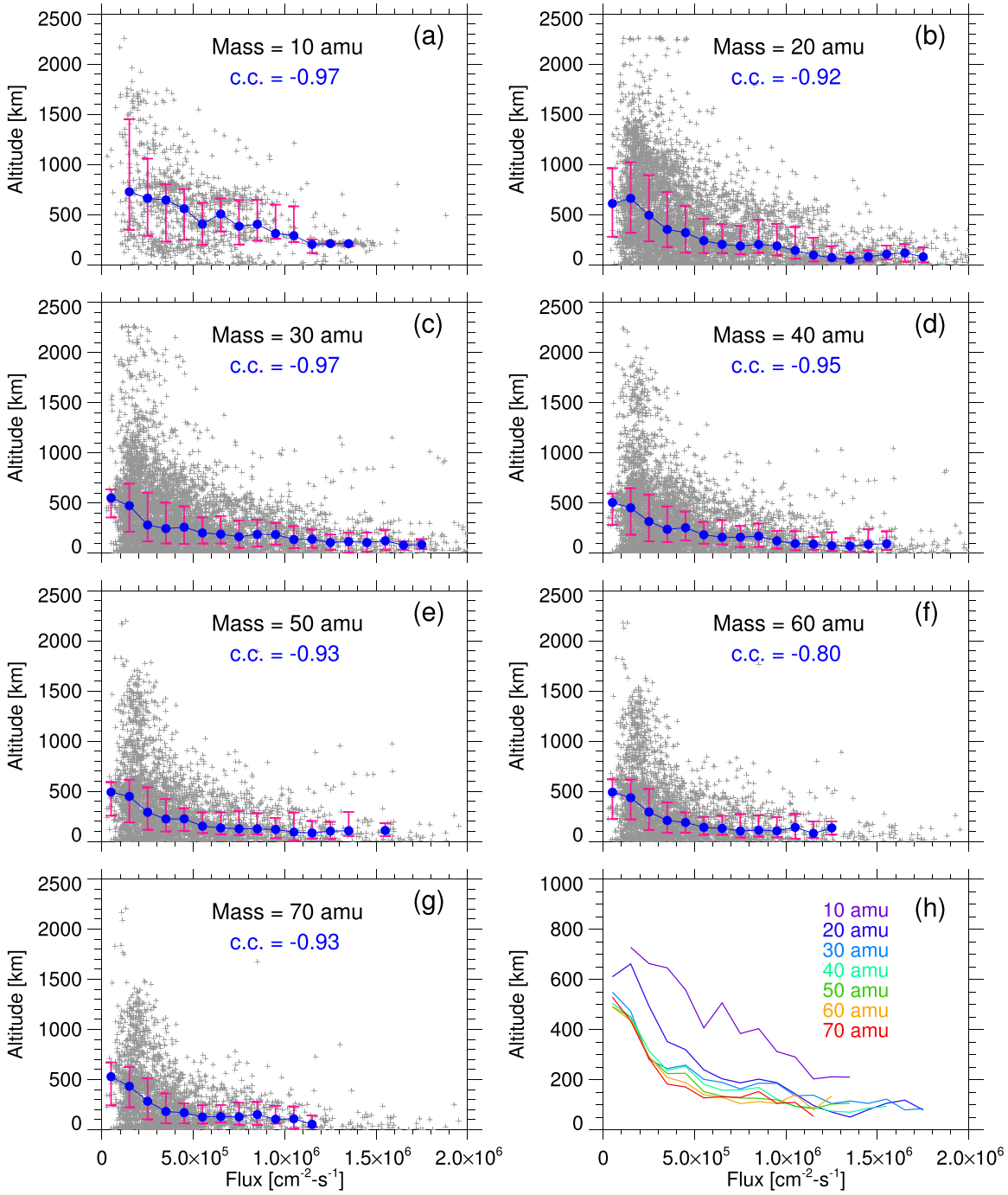

Figure 5. Scatter plots of pickup ion flux vs. source altitude. The format is the same as in Figure 4, but the source local time is replaced by the source altitude.

trend with increasing altitude, leading to a negative relation between the lunar ion flux and altitude. Therefore, once these lunar ions are accelerated by solar wind electromagnetic fields and reach the ARTEMIS spacecraft, we can expect an anticorrelation between the observed flux and source altitude of pickup ions. This anticorrelation would be consistent with our results shown in Figure 5. We further perform a quantitative comparison between pickup ion fluxes observed by the ARTEMIS spacecraft and exospheric ion fluxes estimated by the model, as shown in Figure 6. The ion species included in the model are now categorized according to six assumed mass species ranging from 10–60 amu, with intervals of 10 amu. For example, the exospheric ion flux estimated by the model for mass species of 30 amu takes into account the ion species in the mass range from 25–35 amu. We use the model-estimated flux of each mass species at the subsolar point of each altitude bin for the comparison. The exospheric ion fluxes within each of the six mass bins estimated by the model show a decreasing trend with increasing altitude, and the largest contribution to the total exospheric flux at any altitude bin comes from ion species with masses of around 30 amu. It should be noted that pickup ion fluxes observed by ARTEMIS at any mass assumption actually cover all potential ion species, which are not limited to a specific mass range. Given an

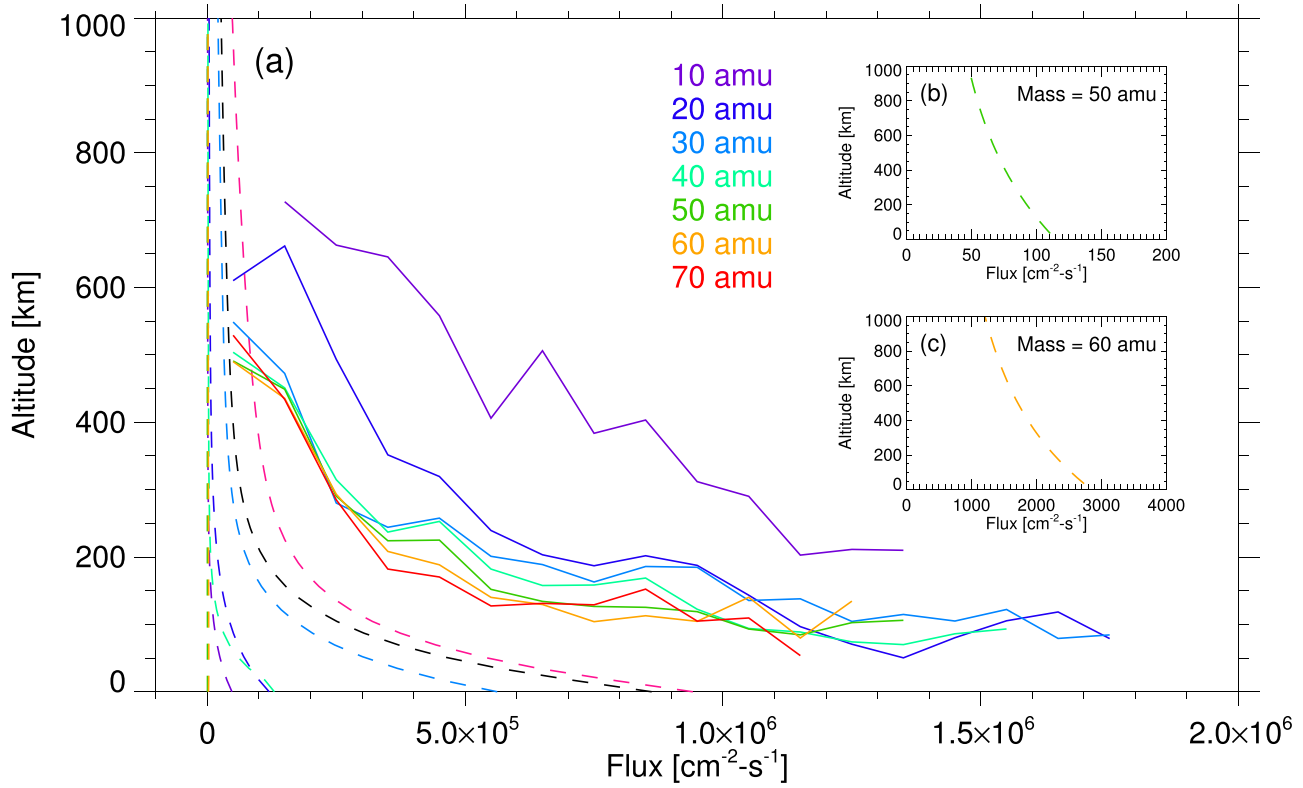

Figure 6. Comparison between pickup ion fluxes observed by ARTEMIS and exospheric ion fluxes modeled by Poppe et al. (2022). The solid curves are the same as the median curves shown in Figure 5, while the dashed curves indicate the model-estimated exospheric ion fluxes. Different colors represent different mass species. The black-dashed curve indicates the total flux of modeled exospheric ions (23 species) with masses between 5 and 65 amu. Compared to the black-dashed curve, the pink one indicates the total flux of all modeled exospheric ions (25 species). (b) and (c) show different flux scales to highlight the variations in the model-estimated fluxes for mass species of 50 and 60 amu, respectively.

assumed mass at an altitude, it is therefore reasonable to see that the pickup ion flux observed by ARTEMIS (solid curves) is much larger than the exospheric ion flux estimated by the model (dashed curves).

In Figure 6, the black-dashed curve indicates the total flux of modeled ion species (23 species) within the mass range between 5 and 65 amu, while the pink-dashed curve indicates the total flux of all modeled ion species (25 species). Compared to the black-dashed curve, the pink one has additional contributions from H_2^+ and He^+ (both species with masses below 5 amu). We find that the total flux of exospheric ions estimated by the model (regardless of black- and pink-dashed curves) is apparently lower than the observed flux of pickup ions for any mass assumption. This quantitative discrepancy can be ascribed to some potential factors outlined below: (1) The first is the inclusion of background ion fluxes within the energy and angular ranges of pickup ions in our calculations of observed pickup ion fluxes. However, as the example shown in Figure 1(d), these background fluxes (at times of 12:10–12:20 or 12:40–12:50) are much smaller than pickup ion fluxes (at times between the two orange vertical lines). (2) The second factor can be attributed to the presence of some ion species in the exosphere that are not considered by the model. For example, they did not include an ion contribution from exospheric H_2O in the model. In addition, Poppe et al. (2022) have pointed out that their comparison to average pickup ion fluxes observed by ARTEMIS demonstrated insufficient model fluxes and furthermore identified CO_2^+ as a potential species underestimated by their model. (3) The numerical model can easily have several uncertainties, such as constraints on the density and spatial distribution of various species and variations in the source functions for the lunar exosphere (e.g., solar wind conditions and micrometeoroid influx). It is thus reasonable for the model to possibly scale the values of some quantities by a factor of multiples. (4) Our analytical trajectory calculations assumed that the pickup ion flux of each observation sample entirely originates from the same location for a given mass. In other words, this quantitative comparison is made under an ideal assumption that the flux of lunar ions remains constant during their movement of being picked up by the solar wind. Taking into account the above possible factors, it is difficult for the model and observation results to be well consistent in magnitude; however, both suggest a decreasing trend of the exospheric ion flux with increasing altitude.

4.3. Dependence on Crustal Magnetic Field Intensity

Halekas et al. (2016) used fully time-dependent charged particle tracing to analyze a multi-minute pickup ion event observed simultaneously by the two ARTEMIS probes. The various pickup ion observation samples in that event were traced back to areas with a wide sunlit local time range above the southern hemisphere of the Moon. They approximately deduced the ion production rate at the source location of each pickup ion observation sample along the analytically described trajectory. Their result shows an apparent local time asymmetry in the production rate, with a higher production rate on the dusk side than on the dawn side. One of their explanations for this result relies on the difference in the crustal magnetic field

intensity between the two local time sectors of the southern hemisphere, with magnetic anomalies on the dawn side. The reflection rate of solar wind protons was found to positively correlate with the local intensity of the crustal magnetic field (e.g., Lue et al. 2011; Saito et al. 2012; Poppe et al. 2017). Therefore, crustal magnetic anomalies are believed to locally diminish the sputtering efficiency of the lunar surface by decelerating and/or partially reflecting solar wind protons before they strike the surface (Wieser et al. 2010; Vorburger et al. 2012; Futaana et al. 2013; Poppe et al. 2014). The production rate of lunar ions could be locally reduced, due to the local suppression in the formation of neutrals. Some freshly born ions near the surface may also be trapped by crustal magnetic fields. As a consequence, the flux of pickup ions originating from a region with the crustal magnetic anomaly may be lower than that originating from a region without the anomaly. For example, Yokota et al. (2020) showed a negative correlation of crustal magnetic field intensities with pickup carbon ion (C^+) fluxes detected by the Kaguya spacecraft at an altitude of about 100 km.

In order to verify the expected effect of crustal magnetic anomalies stated above, we statistically examine the relationship between the observed flux of pickup ions and the crustal magnetic field intensity at the source location. In this investigation, only pickup ion observation samples with source altitudes below 100 km are included because crustal magnetic fields only have significant magnitudes at altitudes close to the lunar surface. Figure 7 shows scatter plots of the two variables for seven different ion mass species. Since most crustal magnetic field models only provide two-dimensional intensity maps as a function of longitude and latitude at a given altitude, we can only project each source location vertically onto a map of crustal magnetic field intensities to estimate its corresponding intensity. The map used in the present study was modeled by Tsunakawa et al. (2015), which shows the intensities at the lunar surface. For each mass species, we calculate the median crustal magnetic field intensity at each flux bin containing at least 20 data points. Because of the additional restriction on the source altitude, there are fewer data points (compared to Figures 4 and 5) that can be analyzed here, especially for the assumed mass of 10 amu. As displayed in Figure 7(a), there are insufficient data points for calculating any median value in this panel, but we still do not see any visible relationship or trend from this scatter plot of fluxes versus crustal magnetic field intensities. For the other six mass species, none of the median curves exhibit a clear relationship between the two examined variables. The Spearman rank correlation coefficients mostly have small magnitudes, and their associated p-values are all larger than 5%, indicating no significant statistical correlations. We have also tried crustal magnetic field intensities at an altitude of 30 km for the same examination stated above, but the results are not much different.

The lack of dependence we obtained from Figure 7 seems inconsistent with the negative correlation reported by Yokota et al. (2020). However, as mentioned previously, pickup ion fluxes observed by the ARTEMIS spacecraft at any mass assumption actually cover a variety of ion species, while Yokota et al. (2020) only examined pickup carbon ion (C^+) fluxes observed by the Kaguya spacecraft. As shown in Figure 2(c), pickup ion fluxes observed by ARTEMIS are mostly much larger than 10^5 cm^{-2} s^{-1}, while the pickup carbon ion fluxes observed by Kaguya are almost smaller than this flux level. This implies that the effect of crustal magnetic anomalies on reducing the local production rate of lunar ions may only work for a few specific ion species, rather than all ion species. On the other hand, the observation altitudes of ARTEMIS were much higher than those of Kaguya. Pickup ions with a longer trajectory may experience a few variations in their fluxes during the movement before reaching the spacecraft, possibly reducing the significance of influences by crustal magnetic anomalies. In addition to this, there are two other factors that could contribute errors in the relation with the crustal magnetic field intensity. One is that the freshly born ions generated from the ionization of neutrals above a crustal magnetic anomaly were considered as originating from the anomaly; the other one is that ions may be deflected by crustal magnetic fields near the surface, leading to errors in determining their corresponding magnetic field intensities. With the possible errors from the factors stated above, the results shown in Figure 7 suggest that the observed fluxes of pickup ions originating from regions with crustal magnetic anomalies are not suppressed as effectively as expected.

5. Summary and Conclusions

This paper presents a statistical study on a set of 115 lunar pickup ion events (containing a total of 11,987 samples) observed by the ARTEMIS spacecraft, pursuing to clarify what factors control lunar pickup ion fluxes. We focus on three factors related to the source location of pickup ions, including the altitude, local time, and crustal magnetic field intensity. To obtain the three parameters corresponding to each pickup ion observation sample, we analytically constructed trajectories in which pickup ions can reach the spacecraft in the correct energy and angle ranges. Because the ESA instruments cannot provide direct information about the mass composition of charged particles, we initially assumed eight mass species (5, 10, 20, 30, 40, 50, 60, and 70 amu) for each pickup ion observation sample to derive possible trajectories. There are no samples that have analytically described trajectories that match ARTEMIS observations under the assumption of a mass of 5 amu. The largest fraction of pickup ion observation samples can have well-matched trajectories at masses of 20 and 30 amu, consistent with previous estimates and observations on pickup ion masses. We investigated the relationship between the pickup ion flux and each of the three source-related parameters stated above for the seven mass assumptions, except for the mass of 5 amu. These different mass assumptions do not lead to different trends in each investigated relationship. Most pickup ion observation samples were traced back to the area around noon regardless of ion fluxes, which can be attributed to the high efficiency of sputtering at the subsolar point. The flux of pickup ions clearly has a strong anticorrelation with the source altitude, consistent with model results and theoretical expectations for altitude variations in the exospheric ion flux and production rate. The relationship between the pickup ion flux and crustal magnetic field intensity does not show the expected anticorrelation. This result implies that any depression of sputtering efficiency or the trapping of near-surface freshly born ions by crustal magnetic anomalies may not effectively reduce pickup ion fluxes as expected. In summary, in addition to the flux of solar wind protons reported in the past

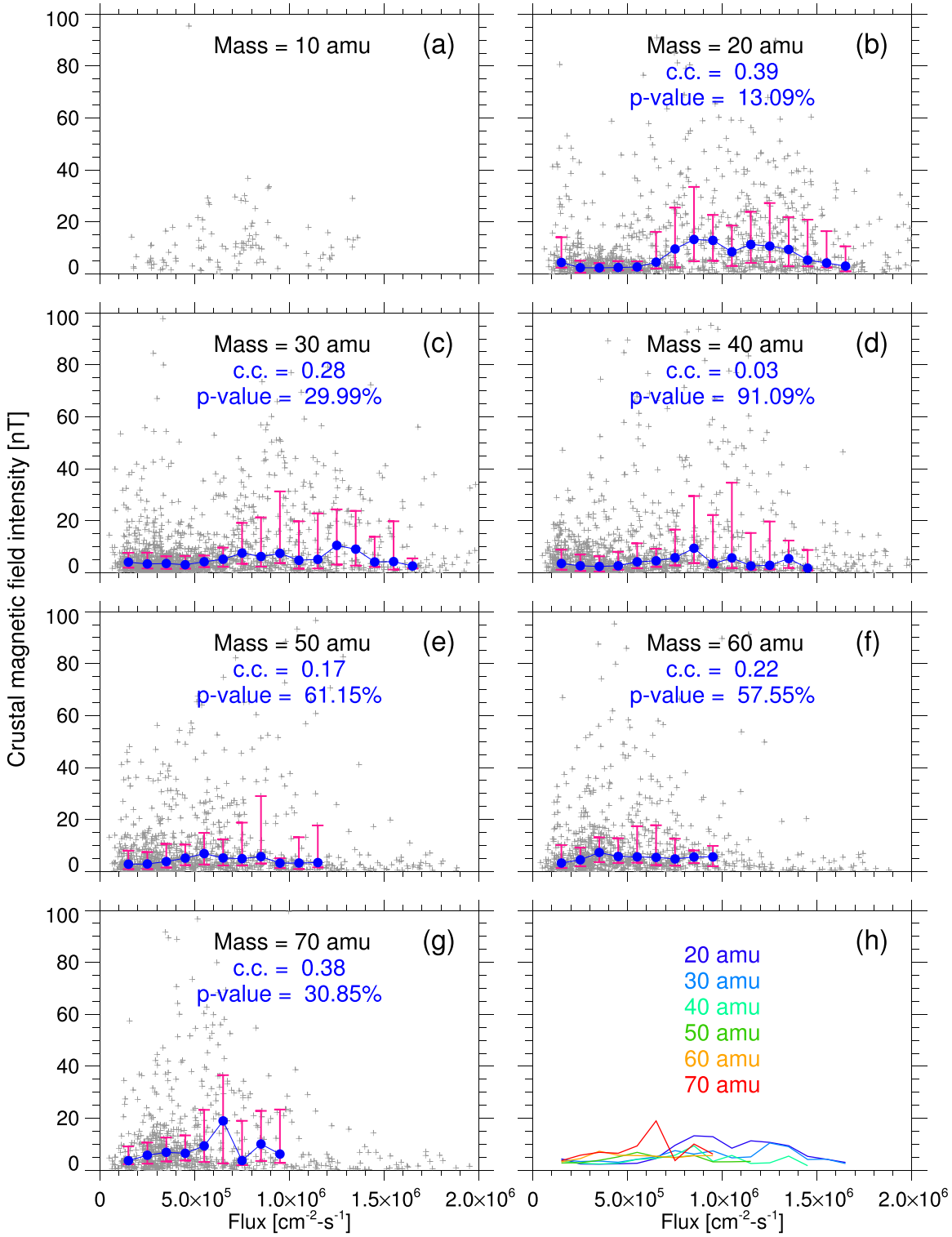

Figure 7. Scatter plots of pickup ion fluxes vs. crustal magnetic field intensities. The format is the same as in Figure 4, but the source local time is replaced by the crustal magnetic field intensity at the surface projected vertically to the source location. These scatter plots include only pickup ion observations that originate from altitudes below 100 km.

(Halekas et al. 2012), the present study suggests that the source altitude plays another general and critical role in controlling the flux of pickup ions. This paper provides a statistical view of the flux of lunar pickup ions as a function of the source altitude, local time, and crustal magnetic field intensity. We believe that the results obtained from the present study will help improve our understanding of the lunar exosphere.

Acknowledgments

The authors acknowledge NASA contract NAS5-02099 and V. Angelopoulos for the use of data from the THEMIS-ARTEMIS Mission. We acknowledge C.W. Carlson and J.P. McFadden for the use of ESA data. We appreciate K.H. Glassmeier, U. Auster, and W. Baumjohann for the use of

FGM data provided under the lead of the Technical University of Braunschweig and with financial support through the German Ministry for Economy and Technology and the German Center for Aviation and Space (DLR) under contract 50 OC 0302. This work was supported by the Solar System Exploration Research Virtual Institute through cooperative agreements 80NSSC20M0022 and 80NSSC20M0060, as well as the Lunar Data Analysis Program through grant 80NSSC20K0311. The two-probe ARTEMIS measurements are all publicly available through the databases themis/thb/l2[3] and themis/thc/l2.[4]

ORCID iDs

Han-Wen Shen https://orcid.org/0000-0001-6733-5065
Jasper S. Halekas https://orcid.org/0000-0001-5258-6128
Andrew R. Poppe https://orcid.org/0000-0001-8137-8176

References

Angelopoulos, V. 2008, SSRv, 141, 5
Angelopoulos, V. 2011, SSRv, 165, 3
Auster, H., Glassmeier, K., Magnes, W., et al. 2008, SSRv, 141, 235
Benna, M., Mahaffy, P., Halekas, J., Elphic, R., & Delory, G. 2015, GeoRL, 42, 3723
Cladis, J., Francis, W., & Vondrak, R. 1994, JGR, 99, 53
Colaprete, A., Sarantos, M., Wooden, D. H., et al. 2016a, Sci, 351, 249
Colaprete, A., Wooden, D., Cook, A., Shirley, M., & Sarantos, M. 2016b, in 47th Lunar and Planetary Sci. Conf., 2635, https://ntrs.nasa.gov/citations/20160003680
Elphic, R., Delory, G., Hine, B., et al. 2014, SSRv, 185, 3
Feldman, P. D., & Morrison, D. 1991, GeoRL, 18, 2105
Flynn, B., & Stern, S. 1996, Icar, 124, 530
Freeman, J., & Benson, J. 1977, PEPI, 14, 276
Futaana, Y., Barabash, S., Wieser, M., et al. 2013, GeoRL, 40, 262
Halekas, J., Benna, M., Mahaffy, P., et al. 2015, GeoRL, 42, 5162
Halekas, J., Poppe, A., Delory, G., Sarantos, M., & McFadden, J. 2013, JGRE, 118, 81
Halekas, J., Poppe, A., Farrell, W., & McFadden, J. 2016, JGRE, 121, 1102
Halekas, J. S., Poppe, A., Delory, G., et al. 2012, JGRE, 117, E06006
Harada, Y., Halekas, J., Poppe, A., et al. 2015, JGRA, 120, 4907
Hartle, R., Sarantos, M., & Sittler, E., Jr. 2011, JGRA, 116, A10101
Hartle, R. E., & Killen, R. 2006, GeoRL, 33, L05201
Hilchenbach, M., Hovestadt, D., Klecker, B., & Möbius, E. 1993, AdSpR, 13, 321
Hodges, R. R., Jr. 2016, GeoRL, 43, 6742
Hoffman, J., Hodges, R., Johnson, F., & Evans, D. 1973, LPSC, 4, 2865
Kuruppuaratchi, D., Mierkiewicz, E., Oliversen, R., et al. 2018, JGRE, 123, 2430
Liuzzo, L., Poppe, A. R., Halekas, J. S., Simon, S., & Cao, X. 2021, GeoRL, 48, e93566
Lue, C., Futaana, Y., Barabash, S., et al. 2011, GeoRL, 38, L03202
Mahaffy, P., Richard Hodges, R., Benna, M., et al. 2014, SSRv, 185, 27
Mall, U., Kirsch, E., Cierpka, K., et al. 1998, GeoRL, 25, 3799
McFadden, J., Carlson, C., Larson, D., et al. 2008a, SSRv, 141, 477
McFadden, J., Carlson, C., Larson, D., et al. 2008b, SSRv, 141, 277
Mendillo, M., Baumgardner, J., & Flynn, B. 1991, GeoRL, 18, 2097
Poppe, A., Halekas, J., Lue, C., & Fatemi, S. 2017, JGRE, 122, 771
Poppe, A., Halekas, J., Samad, R., Sarantos, M., & Delory, G. 2013, JGRE, 118, 1135
Poppe, A., Halekas, J., Szalay, J., et al. 2016, GeoRL, 43, 3069
Poppe, A., Samad, R., Halekas, J., et al. 2012, GeoRL, 39, L17104
Poppe, A., Sarantos, M., Halekas, J., et al. 2014, GeoRL, 41, 4865
Poppe, A. R., Halekas, J. S., & Harada, Y. 2022, JGRE, 127, e2022JE007422
Potter, A., & Morgan, T. 1988, Sci, 241, 675
Rosborough, S., Oliversen, R., Mierkiewicz, E., et al. 2019, GeoRL, 46, 6964
Saito, Y., Nishino, M. N., Fujimoto, M., et al. 2012, EP&S, 64, 83
Saito, Y., Yokota, S., Tanaka, T., et al. 2008, GeoRL, 35, L24205
Sarantos, M., Hartle, R., Killen, R., et al. 2012a, GeoRL, 39, L13101
Sarantos, M., Killen, R. M., Glenar, D. A., Benna, M., & Stubbs, T. J. 2012b, JGRA, 117, A03103
Spearman, C. 1904, Amer. J. Psychol., 15, 72
Stern, S. A. 1999, RvGeo, 37, 453
Szalay, J. R., Horányi, M., Colaprete, A., & Sarantos, M. 2016, GeoRL, 43, 6096
Tanaka, T., Saito, Y., Yokota, S., et al. 2009, GeoRL, 36, L22106
Tsunakawa, H., Takahashi, F., Shimizu, H., Shibuya, H., & Matsushima, M. 2015, JGRE, 120, 1160
Vorburger, A., Wurz, P., Barabash, S., et al. 2012, JGRA, 117, A07208
Vorburger, A., Wurz, P., Barabash, S., et al. 2014, JGRA, 119, 709
Wang, X.-D., Zong, Q.-G., Wang, J.-S., et al. 2011, GeoRL, 38, L14204
Wieser, M., Barabash, S., Futaana, Y., et al. 2010, GeoRL, 37, L05103
Yakshinskiy, B., & Madey, T. 1999, Natur, 400, 642
Yokota, S., Saito, Y., Asamura, K., et al. 2009, GeoRL, 36, L11201
Yokota, S., Saito, Y., Asamura, K., et al. 2014a, P&SS, 93, 87
Yokota, S., Tanaka, T., Saito, Y., et al. 2014b, JGRE, 119, 798
Yokota, S., Terada, K., Saito, Y., et al. 2020, SciA, 6, eaba1050
Zhong, J., Xie, L., Zhang, H., et al. 2013, P&SS, 79, 56
Zhou, X.-Z., Angelopoulos, V., Poppe, A., & Halekas, J. 2013, JGRE, 118, 1766

[3] http://themis.ssl.berkeley.edu/data/themis/thb/l2/
[4] http://themis.ssl.berkeley.edu/data/themis/thc/l2/